

CYCLOSTATIONARY ANALYSIS AND UNSUPERVISED CLUSTERING FOR DETECTING CRACKS IN HELICOPTER GEARBOX CASING

Nader Sawalhi[1], Wenyi Wang1[1]

[1]Platforms Division, Defence Science and Technology Group (DSTG), Australia nader.sawalhi@defence.gov.au, wenyi.wang@defence.gov.au

Abstract

Early detection of structural cracks in helicopter gearbox casings remains a significant challenge, particularly when fault signatures are weak and obscured by operational variability. This study presents a methodology that integrates cyclostationary analysis with unsupervised clustering to detect and monitor crack progression using vibration measurements. The dataset was acquired from a full-scale endurance test of a Bell Kiowa 206B-1 main rotor gearbox conducted at the Defence Science and Technology Group (DSTG), during which a naturally occurring casing crack developed. The spectral correlation function was evaluated at the planet pass frequency to isolate cyclic modulation components associated with crack-induced dynamics. Band-limited energy features were extracted and subsequently analysed using k-means clustering to identify distinct health states without reliance on labelled data. The results demonstrate robust separation of operational conditions and consistent detection of crack evolution across different loads, with early indicators identified well before accelerated fault propagation. The proposed framework enhances sensitivity to incipient faults and offers a reliable approach for condition monitoring of aerospace transmission systems.

Keywords: Cyclostationary analysis, gearbox diagnostics, crack detection, vibration monitoring, clustering

1. Introduction

Vibration-based diagnostics remains a primary approach for monitoring rotating machinery due to its ability to capture small changes in dynamic behaviour associated with fault progression [1]. Established methods perform effectively for gear and bearing defects, where damage generates repeatable spectral components linked to kinematic frequencies. Structural faults such as cracks in gearbox casings present a different challenge. These defects do not introduce distinct excitation frequencies and are often obscured by complex transmission paths and operational variability, particularly at early stages. A casing crack modifies the structural response through local stiffness reduction and intermittent contact at the crack interface. Under cyclic loading, the crack repeatedly opens and closes, producing a time-varying stiffness that introduces nonlinear behaviour into the vibration signal. This mechanism leads to amplitude modulation and frequency coupling, which redistributes energy across the broad spectrum rather than causing localized changes at discrete frequencies. As a result, conventional indicators such as root mean square and kurtosis are often insensitive to early crack development and show strong dependence on operating conditions.

The dynamic behaviour of breathing cracks has been widely studied using simplified structures. Early investigations demonstrated that changes in modal properties can be used to identify crack location and severity [2]. Nonlinear models were later introduced to represent the switching behaviour between open and closed crack states, showing that this mechanism generates harmonic and subharmonic components [3]. Experimental studies confirmed the influence of crack closure on the effective stiffness and vibration response [4], [5]. Further work established that breathing cracks produce modulation effects and nonlinear interactions, resulting in energy transfer across multiple frequency components [6], [7]. While these studies provide important insight, they are largely based on controlled laboratory conditions and do not reflect the complexity of real transmission systems.

https://doi.org/10.71945/icas2026_0019

In planetary gear systems, the loading applied to the casing is periodic and governed by the planet pass frequency. The breathing behaviour of the crack is therefore synchronised with this frequency, introducing modulation into the vibration signal. These modulation effects are not directly observable in conventional spectral representations, as they are embedded within broadband response and influenced by load variation. Cyclostationary analysis [8] provides a suitable framework for detecting such behaviour by explicitly analysing periodic variations in signal statistics. By examining the signal at specific cyclic frequencies, it becomes possible to isolate modulation components associated with physical processes such as crack breathing. This approach directly targets the underlying mechanism that governs the vibration response, forming the basis for the feature extraction process adopted in this study. However, the presence of modulation features alone does not ensure reliable prognostics. To address this, the present work integrates cyclostationary analysis with an unsupervised clustering framework. Features derived at the planet pass frequency are used to characterise the evolution of the system, while clustering is employed to partition the data into distinct operational states. This combined approach provides both physically interpretable indicators and a data-driven mechanism for state identification. The main contribution of this paper is the demonstration that modulation features extracted at a physically meaningful cyclic frequency can be consistently organised into stable health states across varying load conditions, enabling reliable detection and tracking of casing crack progression in a complex gearbox system.

The availability of representative datasets that capture crack evolution under operational loading remains limited. The HUMS2025 dataset [9], developed through a full-scale endurance test conducted by the Defence Science and Technology Group, provides a unique case in which a fatigue crack developed in a helicopter gearbox casing during operation. The dataset includes repeated load cycles and captures the interaction between structural response, excitation mechanisms, and measurement noise, offering a realistic basis for evaluating diagnostic approaches.

2. Test Description

The experimental data analysed in this study were obtained from a full-scale helicopter gearbox endurance test conducted by the Defence Science and Technology Group. The test platform consists of a Bell 206B-1 Kiowa main rotor gearbox, which incorporates both a spiral bevel stage and a planetary reduction stage. The bevel stage includes a 19-tooth pinion driving a 71-tooth bevel gear, while the planetary stage comprises a 27-tooth sun gear, 35-tooth planet gears (4 planets), and a 99-tooth ring gear. This configuration reflects a typical rotorcraft transmission system, where load distribution and structural response are strongly coupled. The original objective of the endurance test was to monitor the progression of a seeded gear tooth fault introduced into the pinion. During the course of testing, an unanticipated fatigue crack developed within the gearbox casing (Figure 1.a). The crack initiated at the spline interface used to secure the ring gear and subsequently propagated toward the casing support region (Figure 1.b). Evidence suggests that additional cracking occurred in adjacent areas, leading to local structural degradation.

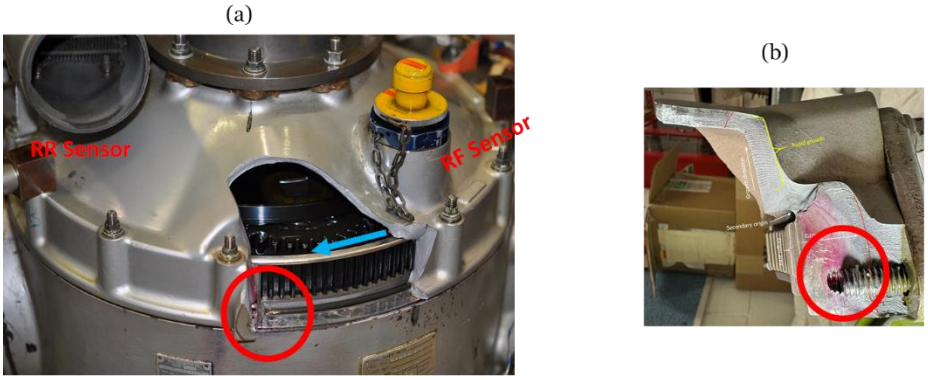


Figure 1 (a) Case after piece detachment (b) Crack Initiation/propagation

Despite the presence of this pre-existing initial damage, the gearbox continued to operate throughout the test period, thereby providing a valuable dataset that captures the evolution of a real structural fault under controlled conditions. This scenario offers a unique opportunity to investigate vibration-based indicators for casing crack detection.

https://doi.org/10.71945/icas2026_0019

The gearbox was instrumented with four accelerometers positioned to capture both gear dynamics and structural response as can be seen in Figure 2. One sensor was mounted on the input pinion (IP), while three sensors were located on the casing in proximity to the ring gear: Ring Front (RF), Ring Left (RL) and Ring Rear (RR). These casing-mounted sensors were positioned near regions of high stress and close to the crack initiation site, which enhances their sensitivity to structural changes.

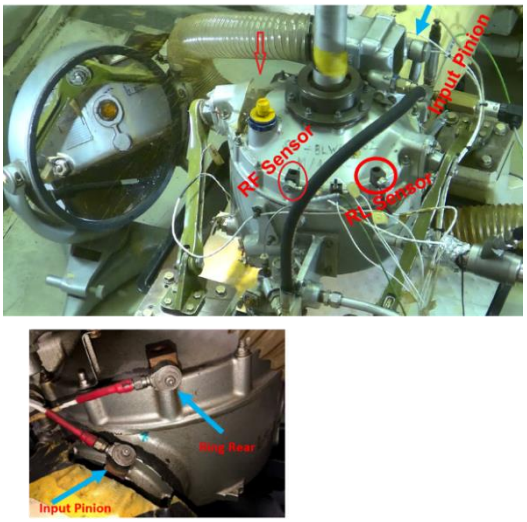


Figure 2 Accelerometers' Locations

Two types of data were distributed for the HUMS2025 Data Challenge. The first consists of hunting-tooth synchronous averages, which provide a phase-consistent representation of gear motion. The second comprises raw vibration time series, which retain the full broadband response of the system. The raw data were sampled at a rate of 65,573.77 Hz, with each record spanning 30 seconds. The analysis presented in this paper focuses on the steady-state raw vibration data corresponding to load conditions of 100% and 125%.

3. Methodology

3.1 Cyclostationary Analysis

Cyclostationary analysis [10] is based on the principle that certain signals exhibit periodic variation in their statistical properties. In the context of rotating machinery, these variations arise from repetitive mechanical interactions such as gear meshing or cyclic loading associated with structural defects [11]. The foundation of this method is the cyclic autocorrelation function (CAF), which quantifies the periodic correlation of a signal $x(t)$ at a specific cycle frequency α and time lag τ. It is defined as:

$$R_x^{\alpha}(\tau) = \lim_{T\to\infty} \frac{1}{T} \int_{-T/2}^{T/2} x\left(t+\frac{\tau}{2}\right) x^*\left(t-\frac{\tau}{2}\right) e^{-j2\pi\alpha t} dt \tag{1}$$

where $x^*(t)$ represents the complex conjugate of $x(t)$. By applying the Fourier transform to the CAF with respect to τ, the spectral correlation function (SCF), or cyclic spectrum can be derived as:

$$S_x^{\alpha}(f) = \int_{-\infty}^{\infty} R_x^{\alpha}(\tau) e^{-j2\pi f\tau} d\tau \tag{2}$$

The SCF reveals periodic structures in the signal that are not detectable using conventional power spectral density (PSD) analysis. When α=0, the SCF reduces to the classical PSD; however, for non-zero α, it highlights cyclic components such as gear mesh harmonics, amplitude modulation, and frequency modulation. This makes cyclostationary analysis particularly powerful for applications such as gearbox diagnostics, bearing fault detection, and communication signal analysis. In practice, the SCF is efficiently computed by segmenting the time signal, applying fast Fourier transform (FFT)-based processing, and averaging the results to form the SCF matrix. This approach is computationally feasible for large datasets. In this study, the analysis is focused on the cyclic frequency corresponding to the planet pass frequency (PPF), i.e. number of planets times the carrier frequency. This choice is motivated by the physical behaviour of the crack, which experiences repeated loading cycles at this

https://doi.org/10.71945/icas2026_0019

frequency. As a result, modulation components associated with crack activity are expected to be concentrated at this cyclic frequency.

3.2 Feature Extraction

The spectral correlation function (SCF) was computed for each vibration signal, and the cyclic spectrum at the selected cyclic frequency (PPF) was extracted and compared with File #1 in the dataset from Day 3 of testing, which served as the reference condition. Amplitude differences were expressed in decibels (dB) relative to 1×10^{-9} m/s2, representing the positive deviation from the Day 3 baseline. This normalization facilitates the identification of changes in the frequency spectrum over time. To improve interpretability, a single trending parameter was derived from these spectral differences. First, the point-wise difference (δ) between the SCFs at the PPF was computed. The resulting amplitude differences (in dB) were then squared to capture variations in spectral energy. These squared differences were integrated across the frequency range, scaled by the discrete Fourier transform (DFT) length (NFFT), and normalized by the Nyquist frequency (0.5 f_s) to account for differences in spectral resolution and bandwidth. Finally, the square root of this value was taken to obtain the Root Mean Square Energy Difference (RMSED). This metric provides a compact representation of the overall energy variation between spectra, enabling more effective tracking of gradual system changes and potential damage progression over time. The RMSED is defined in Equation (3) as:

$$RMSED = \sqrt{\frac{N_{fft} \times \sum_0^{f_s/2} (\delta)^2}{(\frac{f_s}{2})}} \tag{3}$$

Where,
N_{fft}: DFT length (samples)
f_s: Sampling frequency (Sample/s)
δ: Point-wise difference between the SCFs at the PPF

3.3 Unsupervised Clustering

To associate the extracted features with stages of the casing crack growth the extracted features, an unsupervised clustering approach is employed. K-means clustering [12] is selected due to its simplicity and effectiveness in partitioning data into distinct groups. The use of K-means++ initialization improves convergence by providing well-distributed initial cluster centres. The clustering process groups feature vectors into a predefined number of clusters, which are interpreted as representing different operational states. In this study, three clusters are considered, corresponding to normal operation, transitional behaviour, and fault conditions. The quality of clustering is assessed using silhouette analysis, which quantifies the degree of separation between clusters.

4. Results

4.1 Cyclic Spectral Characteristics

Figure 3 and Figure 4 show the power spectral density (PSD) comparison at the PPF cyclic frequency (α = 4 × carrier frequency) for 100% and 125% load, respectively. The cyclic spectral analysis reveals distinct trends in the spatial and frequency-dependent energy distribution. Under both loading conditions, significant activity is concentrated within the frequency range of approximately 1 to 5 kHz, particularly for the casing-mounted sensors (RF, RR, and RL). Among these, the sensors located closest to the crack region (RF and RR) exhibit the most pronounced response, with clear bands of elevated energy that persist and intensify over successive measurements (or File numbers). These features indicate strong modulation effects at the selected cyclic frequency, consistent with crack-related excitation mechanisms.

At the 100% load condition (Figure 3), the overall energy levels are moderate, but coherent patterns are already observable. The RF and RR sensors show localized regions of increased PSD difference that gradually expand over time, while the RL sensor exhibits a weaker but still discernible response within the same frequency band. The IP sensor, in contrast, displays comparatively diffuse and lower-amplitude activity, suggesting reduced sensitivity to the fault at this measurement location.

 https://doi.org/10.71945/icas2026_0019

At the 125% load condition (Figure 4), the cyclic spectral features become significantly more pronounced. The energy levels increase substantially, particularly for the RF and RR sensors, where strong, continuous ridges emerge in the 1–5 kHz range and extend across a larger portion of the dataset. These ridges intensify progressively with increasing File #, indicating accelerated crack growth under higher load. The RL sensor shows moderate enhancement compared to the 100% case, although the response remains less dominant than that of RF and RR. The IP sensor continues to exhibit the weakest response, with energy increases that are less structured and of lower magnitude.

Overall, while the RMSED are lower at 100% load, the underlying trends and spatial distribution patterns remain consistent across both loading conditions. This consistency demonstrates the robustness of the cyclic spectral features for fault detection. However, the higher load condition (normally not used in real operations) enhances both the amplitude and clarity of the spectral signatures, enabling earlier and more reliable identification of crack progression.

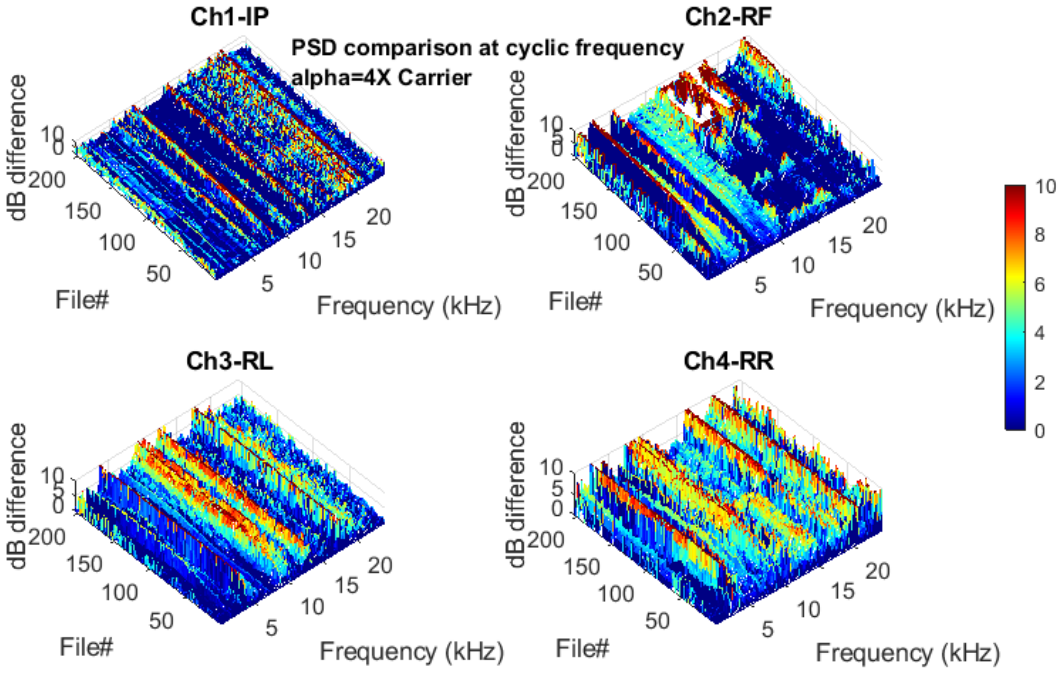


Figure 3 Power Spectral Density comparison at cyclic frequency alpha= planet pass frequency (4xCarrier) for the 100% load

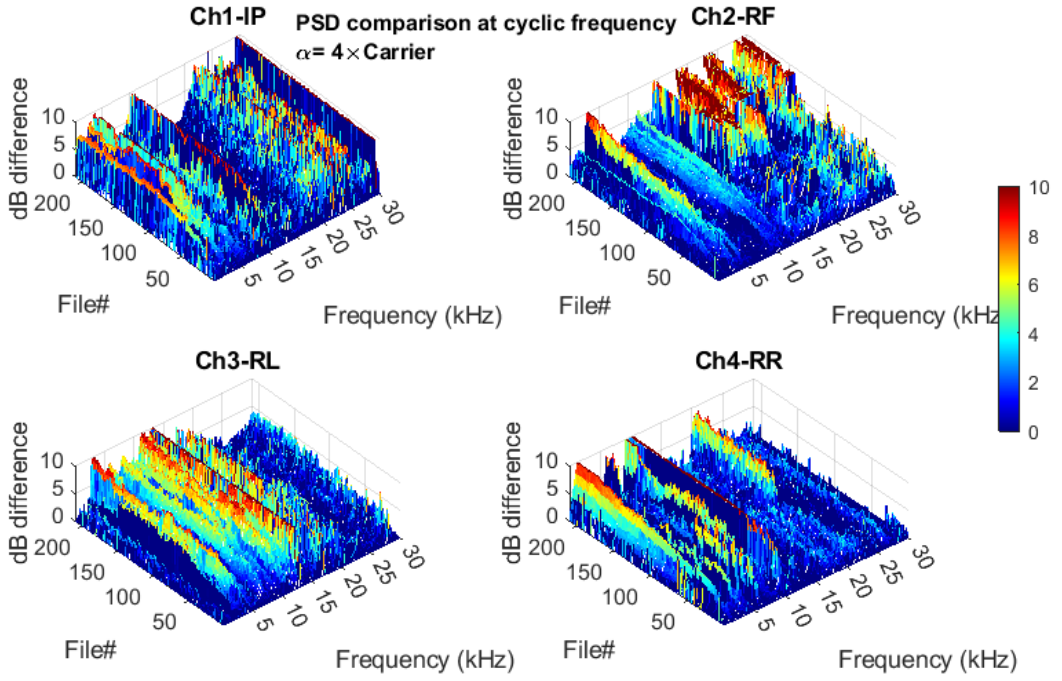


Figure 4 Power Spectral Density comparison at cyclic frequency alpha= planet pass frequency (4xCarrier) for the 125% load

https://doi.org/10.71945/icas2026_0019

4.2 Band-Limited Energy Trends

The narrow band analysis provides further insight into the spatial and frequency-dependent behaviour of the system. Figure 5 presents power spectral density (PSD) comparisons at the PPF cyclic condition (rms dB trending) at 100% load for three different frequency bands. Note that 2×GMF and 4×GMF band analysis are used here due to the use of 4-planet arrangement where 2 pairs of diametric opposing planets give rise to multiples of 2×GMF

The band around 2×GMF (772.4–1,543.9 Hz) shows the most consistent monotonic increase for the rear right (RR) sensor, indicating that this location is particularly sensitive to fault progression in this frequency range. The trend begins near baseline values and steadily increases to approximately 0.7–0.8 dB by file #180–200, demonstrating good correlation with damage evolution. In contrast, the front right (RF) and input pinion (IP) sensors show moderate increases, while the rear left (RL) sensor remains close to zero, suggesting limited sensitivity.

The mid-frequency band (1,800–3,086 Hz), associated with approximately 4×GMF, shows the strongest monotonic behaviour for the RF sensor, which exhibits a steady increase from near 0 dB to approximately 1.8–2 dB. The RR sensor shows an early increase but then plateaus and slightly declines, indicating reduced diagnostic stability compared to RF in this band. The IP sensor shows a mild upward trend, while RL again remains largely unresponsive.

The high-frequency band (13,887–23,659 Hz) shows a distinctly different behaviour pattern. In this band, the RF sensor dominates, exhibiting a sharp increase after file ~120 and reaching peak values close to 9–10 dB before slightly declining toward the end. This suggests strong sensitivity to high-frequency fault-induced energy, likely associated with localized surface damage or impacts. Meanwhile, the IP, RL, and RR sensors show minimal variation, remaining relatively flat around 1–2 dB, indicating low responsiveness at these frequencies.

Overall, these results highlight that fault detectability is highly dependent on both sensor location and frequency band. The RR sensor is most effective near 2×GMF, while the RF sensor provides superior sensitivity at higher harmonics (4×GMF) and particularly in the high-frequency band. The RL and IP sensors show limited diagnostic capability across the evaluated bands, suggesting suboptimal placement or weaker signal transmission paths.

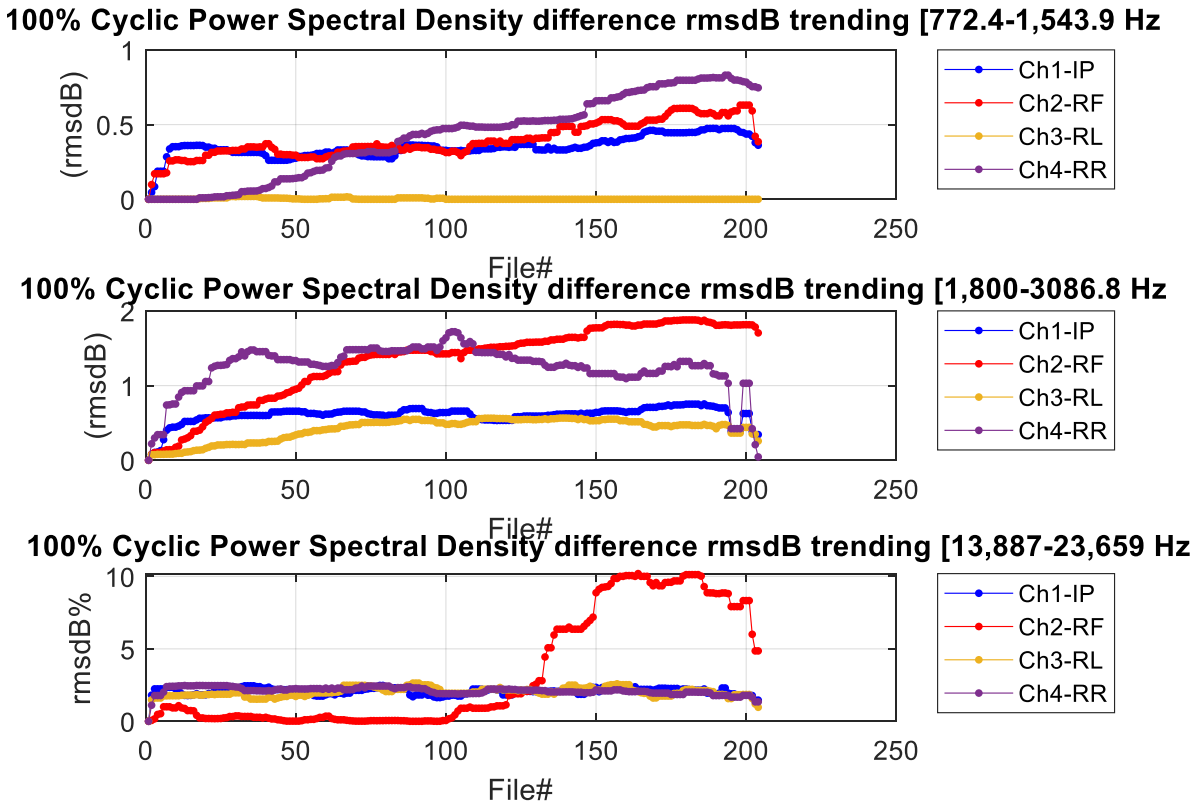


Figure 5 Cyclic Power spectral density difference (rms dB trending) at 100% load top: band 772.4-1,543.9 middle: 1,800-3,086. Hz bottom: 13,887-23,659

At 125% load (Figure 6), the narrow band analysis shows improved separation between sensor

https://doi.org/10.71945/icas2026_0019

responses and clearer fault progression, with earlier onset and higher amplitudes compared to the 100% load case.

In the 2×GMF band (772.4–1,543.9 Hz), the RR sensor again exhibits the most consistent monotonic increase, rising steadily from near 0 dB to approximately 1.2–1.3 dB by the end of the dataset. The increase becomes more pronounced after the marked points around files ~67, ~107, and ~150, indicating progressive fault development. The IP and RF sensors show moderate but stable increases, reaching approximately 0.4–0.6 dB, while the RL sensor remains largely insensitive with only minor variation. Compared to 100% load, the RR trend is both steeper and more clearly defined.

In the mid-frequency band (1,800–3,086 Hz), both the IP and RF sensors demonstrate strong and consistent monotonic growth, reaching peak values of approximately 1.2–1.3 dB. The RF sensor shows slightly better stability at later stages, while the IP sensor exhibits a rapid early increase followed by a plateau. The RL sensor shows a moderate upward trend but at lower amplitude. In contrast, the RR sensor displays non-monotonic behaviour, with an initial increase followed by a decline and partial recovery, indicating reduced reliability in this band under higher load.

The high-frequency band (13,887–23,659 Hz) shows the most pronounced load-dependent effect. The RF sensor dominates strongly, with a sharp increase beginning shortly after file ~100 and rising rapidly to values near 9–10 dB before slightly declining. This indicates high sensitivity to localized damage mechanisms such as impacts or surface distress under increased load. The annotated points (~67, ~107, ~150) correspond to clear transitions in signal energy, with the largest step change occurring near file ~150. The IP, RL, and RR sensors remain comparatively flat (≈1–2 dB), confirming limited responsiveness at these frequencies.

Overall, the 125% load condition enhances both trend clarity and fault detectability, particularly in the RF sensor at higher frequencies and the RR sensor near 2×GMF. The earlier onset of divergence (from ~file 67 onward) suggests that increased load accelerates the manifestation of fault-related spectral features. As observed at 100% load, the RL sensor remains the least sensitive, while IP shows intermediate performance depending on frequency band.

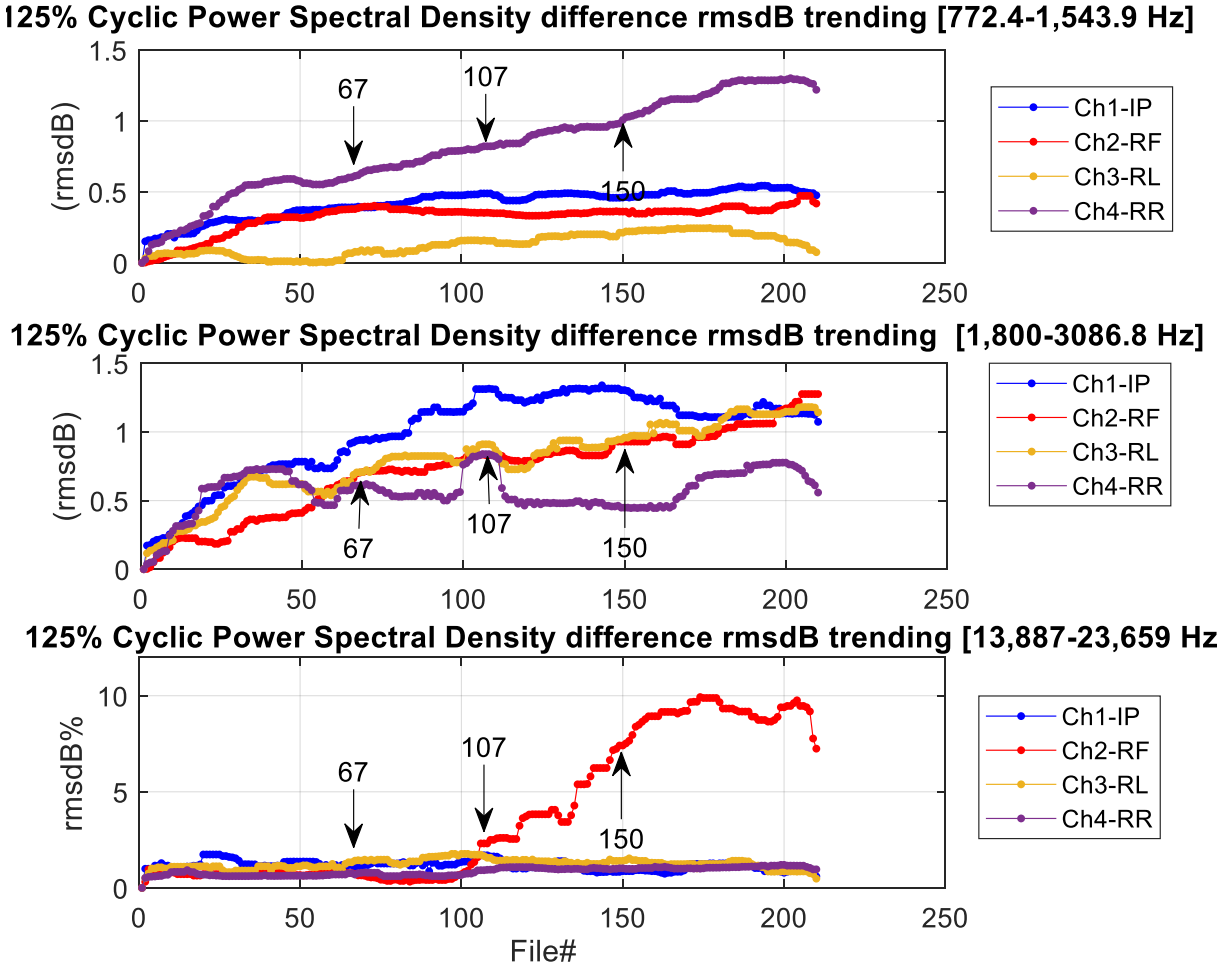


Figure 6 Cyclic Power spectral density difference (rms dB trending) at 125% load top: band 772.4-1,543.9 middle: 1,800-3,086. Hz bottom: 13,887-23,659

https://doi.org/10.71945/icas2026_0019

4.3 Clustering Results

The application of K-means clustering to the extracted features results in a clear separation of operational states into three distinct clusters: normal, transitional, and fault conditions. The transition to the fault state occurs consistently within the test sequence and aligns with the observed crack progression.

The clustering results, supported by the silhouette analysis shown in Figure 7, confirm good cluster validity, with most coefficients remaining above ~0.6. Using the most sensitive indicators—RR in the 2×GMF band (772.4–1,543.9 Hz) and RF in the ~4×GMF band (1,800–3,086 Hz)—the method identifies key degradation milestones: an early warning at day 8 (load cycle 27, ≈ file #55), a clear transition at day 13 (cycle 49, ≈ file #105), and a fault alarm at day 17 (cycle 65, ≈ file #150).

These results demonstrate that the combined cyclic spectral features and clustering approach provides reliable and timely fault detection, with strong alignment to the physical evolution of the crack.

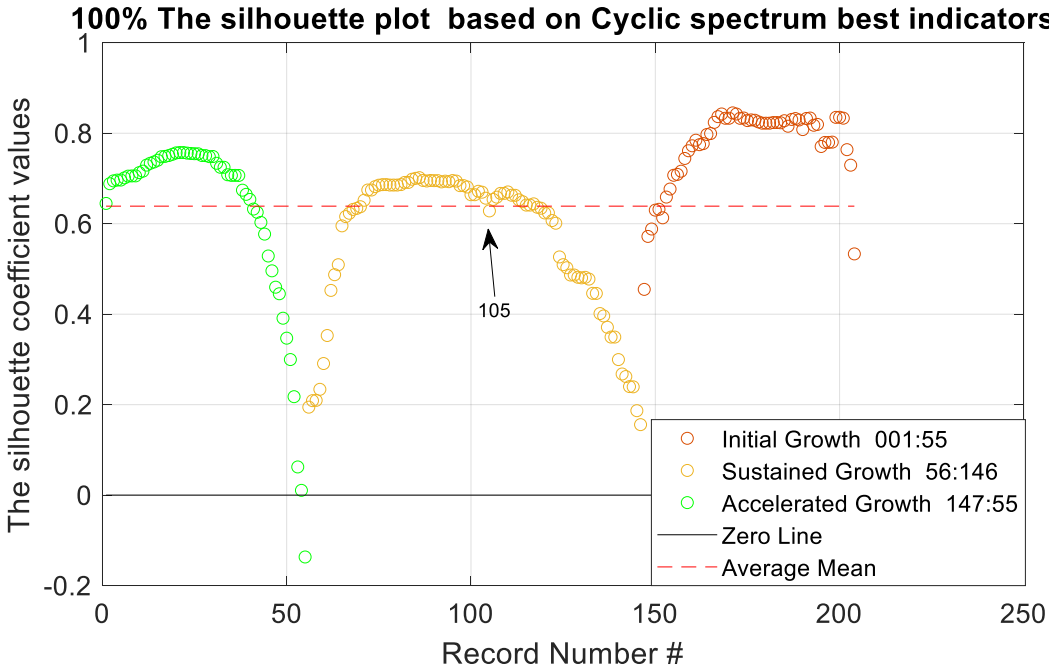


Figure 7 The Silhouette plot based on cyclic spectrum best indicators (RR in the 2×GMF band (772.4–1,543.9 Hz) and RF in the ~4×GMF band (1,800–3,086 Hz)) for the 100% Load

The clustering results for 125% load (Figure 8), based on the most sensitive bands—RR at 2×GMF (772.4–1,543.9 Hz) and RF and RL at ~4×GMF (1,800–3,086 Hz)—show clear separation of degradation stages. The silhouette plot confirms good clustering quality, with most values above ~0.5–0.7.

Key progression points are identified as an early detection at load cycle 31 (≈ file #67), a transition in behaviour at day 13 (load cycle 48, ≈ file #107), and an alarm indicating accelerated growth at day 16 (load cycle 65, ≈ file #150). Compared to the 100% load case, these transitions occur slightly earlier and with stronger separation, reflecting increased sensitivity under higher load.

Overall, the results demonstrate that the approach combining cyclic spectral features and clustering provide robust and timely fault detection, with clear alignment to the physical crack development.

https://doi.org/10.71945/icas2026_0019

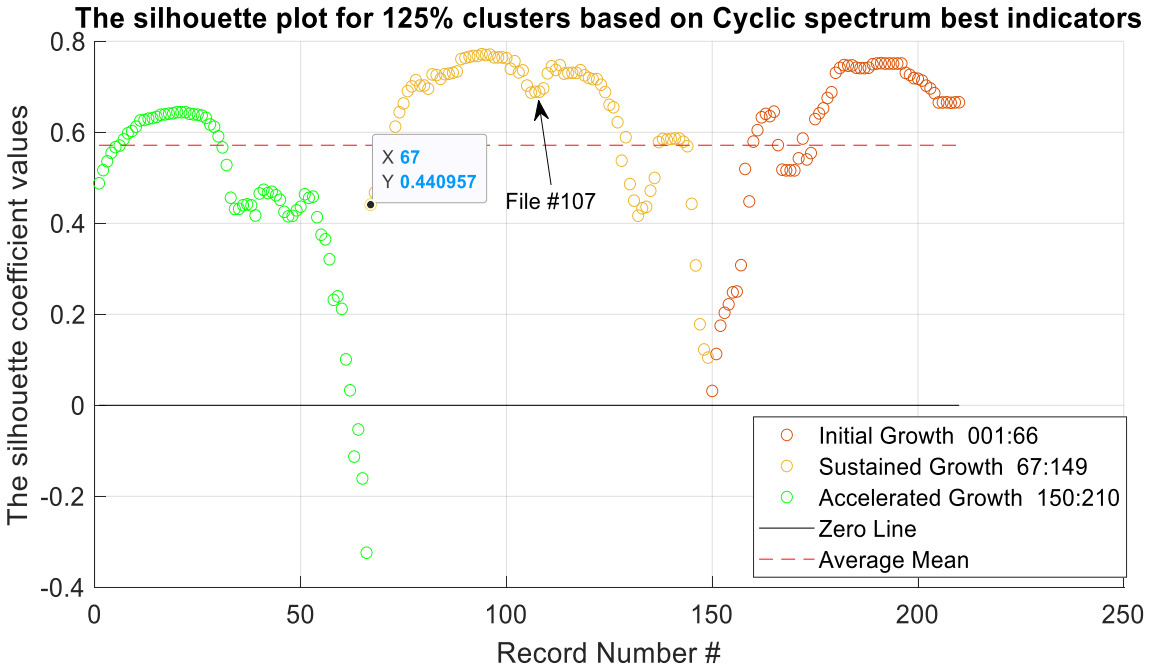


Figure 8 The Silhouette plot based on cyclic spectrum best indicators (RR in the 2×GMF band (772.4–1,543.9 Hz), RF and RL in the ~4×GMF band (1,800–3,086 Hz)) for the 125% Load

5. Discussion

The results demonstrate that cyclostationary analysis provides a significant advantage in detecting crack-induced modulation effects. By focusing on cyclic frequency, the method isolates features that are directly linked to the physical behaviour of the crack. This leads to improved sensitivity compared with conventional spectral techniques.

The integration of clustering further enhances the practical value of the analysis by translating continuous feature trends into discrete health states. This facilitates interpretation and supports decision-making in maintenance applications.

A comparison with traditional indicators such as root mean square, kurtosis, and crest factor reveals that these metrics are often influenced by load variations and may fail to capture early-stage faults. In contrast, the proposed approach maintains consistency across operating conditions and provides a clearer indication of fault progression.

While the method introduces additional computational requirements, these are manageable with modern processing capabilities. The selection of analysis parameters, including frequency bands and clustering configuration, also requires consideration but can be guided by physical insight and validation metrics.

6. Conclusions

This study has presented a methodology that combines cyclostationary analysis with unsupervised clustering for the detection and monitoring of gearbox casing cracks. The results show that modulation features associated with cyclic crack behaviour can be effectively captured at the planet pass frequency. Band-limited energy indicators provide a clear representation of fault progression, while clustering enables reliable separation of system states.

The approach demonstrates consistent performance across different load conditions and offers improved sensitivity to early-stage faults. These characteristics make it well suited for application in condition monitoring systems for rotorcraft transmissions and other rotating machinery.

7. Copyright Statement

The authors confirm that they, and/or their company or organization, hold copyright on all of the original material included in this paper. The authors also confirm that they have obtained permission, from the copyright holder of any third party material included in this paper, to publish it as part of their paper. The authors confirm that they give permission, or have obtained permission from the copyright holder of this paper, for the publication and distribution of this paper as part of the ICAS proceedings or as individual off-prints from the proceedings.

https://doi.org/10.71945/icas2026_0019

8. Acknowledgements

The authors gratefully acknowledge the valuable contributions and support received throughout the Bell 206B MRG pinion gear seeded fault testing project, which led to the development of the casing crack dataset used in the HUMS2025 Data Challenge. We thank the Defence Science and Technology Group (DSTG) test team, Andrew Becker, James Harris, Peter Stanhope, Riyazal Hussein, Jordan Carroll, Brad Bielenberg, Eric Lee, and Anna Houston, whose work in designing and conducting the seeded fault tests was instrumental in generating the dataset. We also acknowledge the crack fractography analysis team, including Vui-Tung Mau and James Niclis (QinetiQ), and Cathy Smith and Nick Athiniotis (DSTG), for their work in assessing and quantifying the fracture surfaces of the casing. Finally, the authors thank the management of the DSTG Platforms Division for their ongoing support of the HUMS Conference series.

References

[1] Jardine A.K.S., Lin D., Banjevic D. A review on machinery diagnostics and prognostics. *Mechanical Systems and Signal Processing*, Vol. 20, No. 7, pp. 1483–1510, 2006.

[2] Rizos, P.F., Aspragathos, N., Dimarogonas, A.D., Identification of crack location and magnitude in a cantilever beam from the vibration modes, *Journal of Sound and Vibration* 138 (3) (1990) 381–388. ISSN 0022-460X, https://doi.org/10.1016/0022-460X(90)90593-O.

[3] Chu, Y.C., Shen, M.H.H., *Analysis of forced bilinear oscillators and the application to cracked beam dynamics*, *AIAA Journal* 30 (1992) 2512–2519. https://doi.org/10.2514/3.11302.

[4] Clark, R., Dover, W.D., Bond, L.J., *The effect of crack closure on the reliability of NDT predictions of crack size*, *NDT International* 20 (1987) 269–275. https://doi.org/10.1016/0308-9126(87)90123-2.

[5] Abraham, O.N.L., Brandon, J.A., *The modelling of the opening and closure of a crack*, *Journal of Vibration and Acoustics* 117 (1995) 370–377. https://doi.org/10.1115/1.2836420.

[6] Chondros, T.G., Dimarogonas, A.D., Yao, J., *Vibration of a beam with a breathing crack*, *Journal of Sound and Vibration* 239 (2001) 57–67. https://doi.org/10.1006/jsvi.2000.3127.

[7] Rezaee, M., Hassannejad, R., *A new approach to free vibration analysis of a beam with a breathing crack based on mechanical energy balance method*, *Acta Mechanica Solida Sinica* 24 (2011) 185–194. https://doi.org/10.1016/S0894-9166(11)60019-0.

[8] Gardner, W.A., *Statistical spectral analysis: A nonprobabilistic theory*, Prentice Hall, 1987. https://cyclostationarity.com/wp-content/uploads/2020/06/Statistical_Spectral_Analysis_A_Nonprobabilistic_Theory.pdf [Note: Book with URL; accessed 09:37 AM AEST, May 1, 2026.]

[9] Defence Science and Technology Group, *HUMS2025 Data Challenge*, Retrieved from https://www.dst.defence.gov.au/our-technologies/hums2025-data-challenge (accessed 09:37 AM AEST, May 1, 2026).

[10] Gardner W.A., Statistical spectral analysis: A nonprobabilistic theory, Prentice Hall, Englewood Cliffs, NJ, USA, 1987.

[11] Antoni J., Bonnardot F., Raad A., El Badaoui M., Cyclostationary modelling of rotating machine vibration signals, Mechanical Systems and Signal Processing, 18(6), pp. 1285–1314, 2004. https://doi.org/10.1016/S0888-3270(03)00088-8.

[12] Arthur D., Vassilvitskii S., k-means++: The advantages of careful seeding, Proceedings of the Eighteenth Annual ACM-SIAM Symposium on Discrete Algorithms, New Orleans, LA, USA, pp. 1027–1035, 2007.

 https://doi.org/10.71945/icas2026_0019